All-Optical Detection of Spin Pumping and Giant Interfacial Spin Transparency in $Co_2Fe_{0.4}Mn_{0.6}Si$/Pt Heterostructure

Koustuv Dutta, Surya N Panda, Takeshi Seki, Santanu Pan, Koki Takanashi, and Anjan Barman*

Active control over the generation and manipulation of pure spin current has propelled drastic transformation in new generation spintronics. Spin pumping is one of the favored mechanisms to generate pure spin current and its efficiency can be parameterized in terms of spin-mixing conductance ($G_{\uparrow\downarrow}$) and spin-diffusion length (λ). Here, using all-optical time-resolved magneto-optical Kerr magnetometry, spin pumping in a ferromagnetic Heusler compound ($Co_2Fe_{0.4}Mn_{0.6}Si$ (CFMS))/Pt heterostructure is investigated keeping in mind the small intrinsic damping and stable spin-polarized band structure at the Fermi level of the CFMS and excellent spin-sink property of Pt. The thickness-dependent evolution of Gilbert damping is modeled using ballistic and diffusive spin transport frameworks to extract $G_{\uparrow\downarrow}$ and λ. Finally, a giant value of interfacial spin transparency up to 0.87 ± 0.02 combined with small intrinsic damping of 0.0039 ± 0.0004 promote the CFMS/Pt heterostructure as a champion material for the development of advanced spin-orbitronic devices.

K. Dutta, S. N Panda, S. Pan, A. Barman
Department of Condensed Matter Physics and Material Sciences
S. N. Bose National Centre for Basic Sciences
Block JD, Sector III, Salt Lake, Kolkata 700106, India
E-mail: a_barman@yahoo.com; abarman@bose.res.in
T. Seki
Institute for Materials Research
Tohoku University
Sendai 980–8577, Japan
T. Seki
Center for Spintronics Research Network
Tohoku University
Sendai 980–8577, Japan
K. Takanashi
Institute for Materials Research
Tohoku University
Sendai 980–8577, Japan
K. Takanashi
Center for Spintronics Research Network
Tohoku University
Sendai 980–8577, Japan
K. Takanashi
Center for Science and Innovation in Spintronics
Core Research Cluster, Tohoku University
Sendai 980–8577, Japan

1. Introduction

Efficient generation and precise manipulation of pure spin current[1] have become pivotal aspects of contemporary spintronics[2] offering a robust mechanism to harness the spin degree of freedom in a myriad of low-dimensional systems.[3,4] As pure spin current consists of the flow of spin angular momentum devoid of net charge transfer, it holds the potential to minimize the Joule heating and Oersted fields[5] in a circuit promising the development of ultra-low-power computing technology. The active manipulation of pure spin current in a ferromagnet (FM)/nonmagnet (NM) thin film heterostructure has three crucial aspects, namely, generation, transport, and absorption.[6] Various physical phenomena such as spin Hall effect (SHE),[7,8] spin caloric effects,[9–12] spin pumping,[13] non-local injection of spin,[14,15] have been utilized for efficient generation of pure spin current in FM/NM heterostructures. Amongst those, spin pumping tenders an elegant method as it is free from the impedance mismatch problem.[16] This mechanism can be quantitatively treated in terms of spin-diffusion length of the NM and spin-mixing conductance[17] associated with the FM/NM interface. Additionally, for spin-orbit torque-based applications, interfacial spin transparency is a salient parameter determining the spin transfer efficiency. Interfacial spin transparency as a function of spin-mixing conductance and spin-diffusion length essentially measures the amount of spin that can effectively pass through the interface.[18] Therefore, from an application viewpoint, a large value of interfacial spin transparency is the key for improved device efficiency.[19]

Very few reports are available in the literature exploring the potential of Heusler compound and heavy metal heterostructure in effective spin current manipulation using spin pumping.[20,21] Cobalt-based Heusler compounds are promising half-metallic materials[22] which gained considerable interest[23] for their application potential in tunnel magnetoresistance (TMR) devices,[24,25] spin-torque nano oscillator (STNO) with low switching current[26,27] etc. They can provide significant edge in the pure spin current manipulation over the other FM materials because of their small intrinsic magnetic damping[28–31] and stable spin-polarized band structure.[32] $Co_2Fe_{0.4}Mn_{0.6}Si$ (CFMS, hereafter) shows high Curie temperature ($\approx$1000 K),[33] low Gilbert damping, (0.004)[29] and its high spin polarization leads to

**ADVANCED
SCIENCE NEWS**
www.advancedsciencenews.com

**ADVANCED
QUANTUM
TECHNOLOGIES**
www.advquantumtech.com

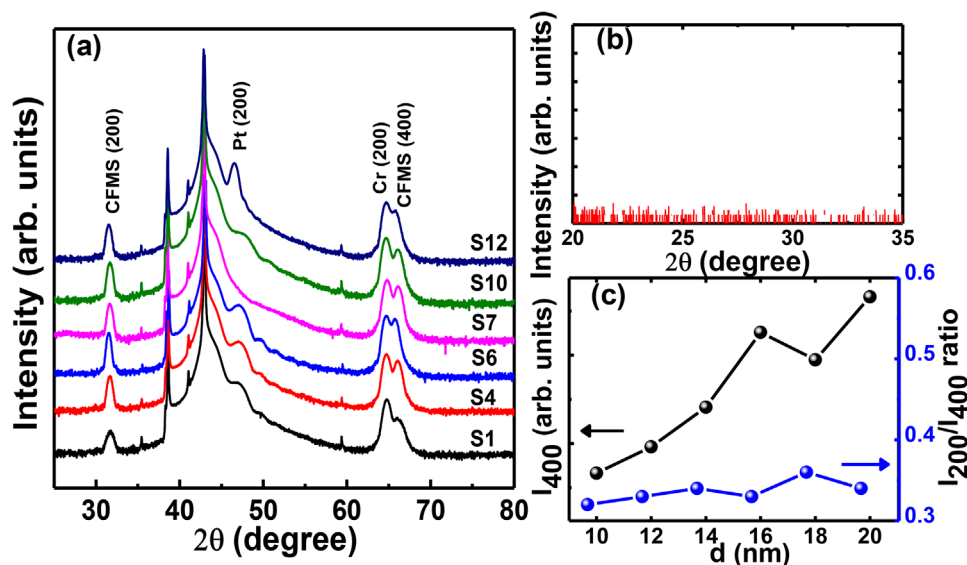**Figure 1.** Crystalline ordering of CFMS from XRD. a) XRD patterns for the MgO (sub)/Cr/CFMS/Pt/Al samples measured in conventional θ–2θ geometry. Intense diffraction peaks from CFMS (200), CFMS (400), and Pt (200) are identified along with Cr (200) peak. b) The tilted XRD scan showing no prominent peak from CFMS (111) indicating the absence of $L2_1$ structural phase. c) Intensity of CFMS (400) diffraction peak is found to increase with CFMS layer thickness whereas the integrated intensity ratio between CFMS (200) and CFMS (400) peaks remains thickness invariant, suggesting a stable Co-atomic site ordering.

superior TMR ratio than its peers. On the other hand, platinum is an archetypal heavy metal with high spin-orbit coupling (SOC) strength,[34] and is popular for its giant spin Hall conductivity, low resistivity, high stability, and efficiency as a spin reservoir in FM/NM heterostructures.

Incidentally, majority of the studies on spin pumping in the literature are carried out by studying inverse spin Hall effect employing all-electrical techniques such as, ferromagnetic resonance (FMR). More recently, the all-optical time-resolved magneto-optical Kerr effect (TRMOKE) has been used as a reliable and non-invasive technique to probe spin pumping including spin-mixing conductance, spin-diffusion length, and interfacial spin transparency in FM/NM heterostructures.[19,35] This technique is devoid of any complex microfabrication of delicate waveguide structures. Besides, local measurement of magnetization dynamics directly in the time domain gives it a significant advantage in precise and reliable determination of magnetic damping parameter over the alternative techniques. Therefore, the objective of this study is to perform unambiguous measurement of spin pumping and related phenomena in CFMS/Pt heterostructures using the all-optical TRMOKE technique and to extract the important parameters as discussed above. From the experimental results, we have extracted the spin-mixing conductance and spin-diffusion length for the CFMS/Pt heterostructure using both the ballistic model[36–38] and the drift-diffusion model of spin transport,[39,40] and thereby the interfacial spin transparency employing two different approaches, namely, the spin-Hall magnetoresistance model[41] and spin-transfer torque based model.[42] Moreover, we have compared the relative contributions from the spin pumping, spin memory loss (SML), and two-magnon scattering (TMS) at the interface to the magnetic damping parameter. This study will substantially enhance the in-depth understanding of the fundamental magnetic properties

of Heusler compound-based FM/HM heterostructures and promote them as a promising candidate for future spin-orbitronic devices.

2. Results and Discussion

In our study two series of films with stacks of MgO(sub)/Cr(20 nm)/CFMS(d)/Pt(t)/Al(2 nm) were prepared. For series I (S1–S6), the nominal CFMS layer thickness was varied as $d = 10$, 12, 14, 16, 18, and 20 nm while maintaining a constant thickness of Pt at $t = 5$ nm. For series II (S7–S12), the Pt layer thickness was varied as $t = 1$, 2, 3, 4, 5, 8, and 12 nm, keeping $d = 16$ nm. Further details can be found in Section 4.

2.1. Structural Characterization

The crystalline phase and atomic-site ordering play non-trivial roles in the determination of the magnetic properties of Heusler compounds.[22,43] Therefore, before proceeding to the investigations of dynamic magnetic properties, we have performed some important structural characterizations of the deposited samples systematically. In **Figure 1**a, XRD data measured in usual θ–2θ geometry are shown for a few representative samples from both series I and II. The presence of a strong diffraction peak from CFMS (400) at 66.3° suggests good crystalline growth of CFMS associated with cubic lattice symmetry, whereas a clear diffraction peak at 31.8° from CFMS (200) strongly indicates the formation of B2 lattice ordering for all the CFMS layers under investigation. A tilted X-ray diffraction (XRD) scan presented in Figure 1b shows no clear CFMS (111) peak, thereby ruling out the possibility of any admixture of $L2_1$ phase in the lattice ordering. Careful

**ADVANCED
SCIENCE NEWS**

www.advancedsciencenews.com

**ADVANCED
QUANTUM
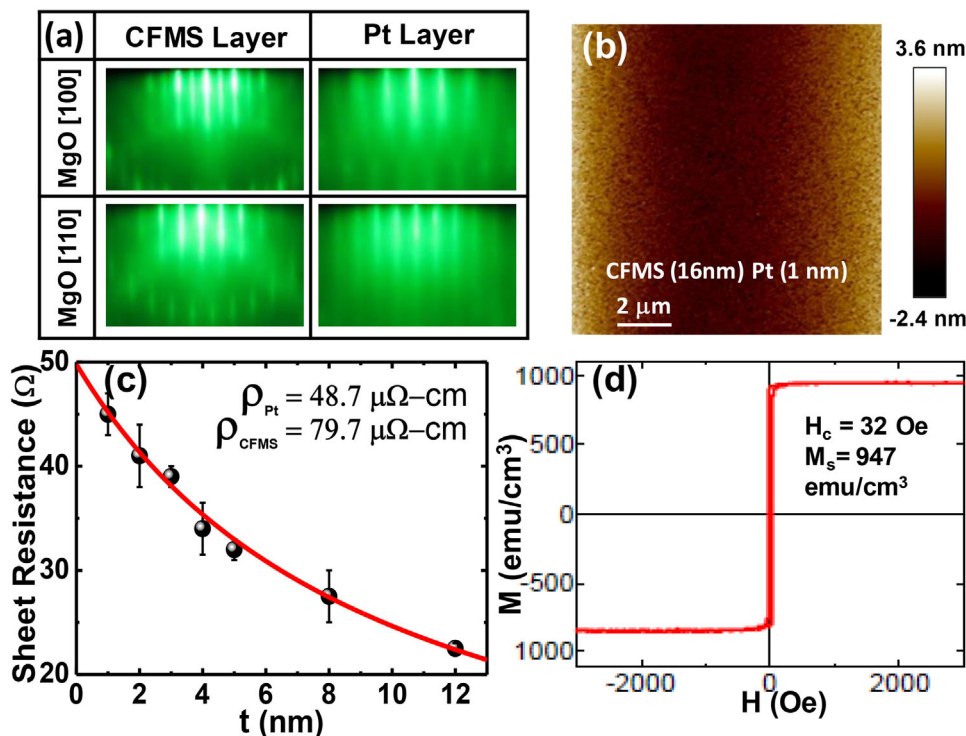TECHNOLOGIES**

www.advquantumtech.com

Figure 2. Determination of structural, magnetic properties, and resistivity. a) In situ RHEED patterns exhibiting clear streaks along MgO [100] and MgO [110] crystallographic directions obtained from CFMS and Pt layers. b) Measurement of mean surface roughness from AFM image. c) Variation of sheet resistance of the heterostructure as a function of Pt layer thickness. d) Representative result of magnetization versus magnetic field from in-plane VSM measurements for S1 sample showing extraction of coercive field and saturation magnetization.

observation reveals that both the intensities of the CFMS (200) and CFMS (400) superlattice peaks are increasing for the case of S1 ($d = 10$ nm) to S3 ($d = 20$ nm) which are in consonance with the increasing nominal thickness. As a previous report[43] presented a thickness dependent ordering for CFMS, we have calculated the integrated intensity ratio of CFMS (200) to CFMS (400) diffraction peaks as shown in Figure 1c. Though an increasing trend in the intensity of CFMS (400) peak signifies an improvement of cubic crystalline structure, the nearly constant value of the integrated intensity ratio confirms a very stable atomic-site ordering of Co-atoms within the compound structure. The degree of lattice strain can also be qualitatively understood from the analysis of Pt (100) peak, which is presented in Section S1, Supporting Information.

To understand the nature of oriented growth of the CFMS and Pt thin film layers along the MgO [100] and MgO [110] directions, in situ reflection high energy electron diffraction (RHEED) images have been acquired. The images for CFMS and Pt layers are depicted in **Figure 2**a for the sample S4. The prominent streaks observed in the images confirm the epitaxial growth of both the CFMS and Pt layers. The CFMS (001) and Pt (001) planes have grown on the MgO (001) plane. In addition, the CFMS [110] and Pt [100] directions have aligned parallel to the MgO [100] direction. Here, the Cr layer acts as a buffer layer which promotes the epitaxial growth of layers by reducing the lattice mismatch between MgO and CFMS layer. Previous studies suggested the achievement of a better crystalline ordering after post-deposition annealing[30,44] which is reconfirmed by the RHEED patterns

from all the samples. From these RHEED observation, we found the following epitaxial relationship: MgO (001) || Cr (001) || CFMS (001) || Pt (001) and MgO [100] || Cr [110] || CFMS [110] || Pt [100].

The atomic force microscopy (AFM) image revealing the surface topography for a particular sample (S7) is presented in Figure 2b. The mean surface roughness calculated over a large area shows a fairly small value of 0.48 nm. The average topographical roughness corresponding to all the samples are of the same order. However, for the heterostructure, interface roughness for the individual layers significantly contributes to the control of the spin transport across the interface. Layer thickness and roughness values estimated from the simulation of X-ray reflectivity measurement data are presented in **Table 1**. For further details, please refer to Section S2, Supporting Information.

Figure 2c displays the variation of the sheet resistance of the heterostructure as a function of the platinum layer thickness. The resistance versus thickness data are fitted using a standard parallel combination of resistance model and the resistivities of the CFMS and Pt layers are calculated to be 79.7 ± 1.1 and 48.7 ± 0.8 $\mu\Omega$ cm, respectively.

2.2. Static Magnetic Properties

The magnetic hysteresis behavior of all samples has been studied using vibrating sample magnetometer (VSM) at room temperature. Figure 2d shows a typical plot of magnetization versus in-plane applied magnetic field of S1 sample along the easy axis

**ADVANCED
SCIENCE NEWS**

www.advancedsciencenews.com

**ADVANCED
QUANTUM
TECHNOLOGIES**

www.advquantumtech.com

Table 1. Coercive field and saturation magnetization values extracted from VSM measurements along with the thickness and roughness values estimated from the XRR measurements for MgO (sub)/Cr(20)/CFMS(*d*)/Pt(*t*)/Al(2) samples.

Sample	Measured from VSM		Nominal thickness		Thickness and roughness extracted from XRR							
					Cr (buffer)		CFMS		Pt		Al (capping)	
	H_c [Oe]	M_s [emu cc^{-1}] ($\pm 2\%$)	CFMS	Pt								
			d [nm]	t [nm]	d' [nm]	σ [nm]	d [nm]	σ [nm]	t [nm]	σ [nm]	d'' [nm]	σ [nm]
S1	32	947	10	5	20.28	0.60	10.15	0.21	5.50	0.39	2.20	0.30
S2	32	902	12	5	20.08	0.30	12.01	0.40	5.70	0.36	2.10	0.60
S3	34	888	14	5	20.28	0.50	14.02	0.28	5.60	0.44	2.00	0.60
S4	30	922	16	5	20.68	0.30	16.01	0.22	6.00	0.45	2.00	0.21
S5	26	868	18	5	20.38	0.59	18.04	0.33	5.85	0.53	2.00	0.50
S6	24	896	20	5	20.58	0.30	20.01	0.21	5.75	0.45	2.00	0.60
S7	24	909	16	1	20.05	0.29	16.00	0.39	1.70	0.33	1.90	0.69
S8	33	875	16	2	20.35	0.33	15.97	0.27	2.84	0.47	1.29	0.68
S9	22	923	16	3	20.56	0.42	16.20	0.31	3.70	0.48	2.73	0.48
S10	30	871	16	4	20.06	0.22	16.10	0.21	4.78	0.35	2.33	0.38
S11	22	856	16	8	20.94	0.30	15.80	0.32	8.90	0.45	2.01	0.35
S12	25	895	16	12	20.44	0.20	15.20	0.29	12.50	0.45	2.00	0.26

of CFMS ([110] direction) which reveals a square hysteresis loop for the sample. The estimated saturation magnetization (M_s) and coercive field (H_c) values for all samples are presented in Table 1. The M_s values differ slightly from one another and show about 10–18% reduction from the bulk value of 1050 emu cc^{-1}.[43,45] The H_c values for the samples are found to be small having an upper bound of ≈ 35 Oe.

2.3. Investigation of Damping Constant from All-Optical TRMOKE Measurement

The phenomenon of spin pumping at the CFMS/Pt interface is schematically depicted in **Figure 3**a along with the optical pump-probe measurement geometry. A typical TRMOKE result presented in Figure 3b comprises of signatures from different physical phenomena associated with a magnetic system in the femtosecond to nanosecond timescale. When an ultrashort laser pulse is incident upon a ferromagnetic surface, a sudden drop in magnetization is observed referred to as the ultrafast demagnetization.[46] The magnetization then exhibits a recovery via spin-lattice relaxation giving rise to the fast relaxation process. The third regime essentially consists of the slow relaxation process superimposed with spin precession where the energy is redistributed from the system to the surroundings and the system reclaims its initial magnetization.[47] To find the magnetic damping, it is imperative to calculate the effective magnetization and the characteristic decay time associated with the precession of spins. To execute this, the precessional Kerr oscillations, after eliminating the bi-exponential background caused by the relaxation, are fitted with a sinusoidal function with decaying amplitude of the following form

$$\theta_k (t) = A e^{-\frac{t}{\tau}} sin (2\pi \nu t + \varphi) \tag{1}$$

where τ is the decay constant of the spin precessional motion with frequency ν and amplitude A.

Time-resolved Kerr oscillations are measured at different strengths of the bias magnetic field and the corresponding frequency values have been calculated from the fast Fourier transform (FFT) spectra. We plot the bias magnetic field dependence of the precessional frequency and the effective magnetization has been extracted for all samples from theoretical fit using the Kittel formula for uniform precessional mode given below[48,49]

$$\nu = \frac{\gamma}{2\pi} \sqrt{\left(H\cos \left(\theta_H - \theta_M \right) + H_a \right) \left(H\cos \left(\theta_H - \theta_M \right) + H_b \right)} \tag{2}$$

where $\gamma = g\mu_B/\hbar$; g, μ_B, and $\hbar$ being the Lande g-factor, Bohr magneton, and reduced Planck's constant, respectively and H represents the bias magnetic field. θ_H and θ_M are the respective angles between in-plane easy axis with the applied bias field orientation and direction of magnetization. H_a and H_b are the contributions from twofold and fourfold anisotropies and are given by[48]

$$H_a = \frac{2K_2}{M_s} \cos 2\theta_M + \frac{2K_4}{M_s} \cos 4\theta_M \tag{3}$$

$$H_b = 4\pi M_s + \frac{2K_z}{M_s} - \frac{2K_2}{M_s} \sin^2 \theta_M + \frac{K_4}{M_s} \left(2 - \sin^2 (2\theta_M) \right) \tag{4}$$

where K_2, K_4, and K_z are in-plane uniaxial, cubic crystalline, and out-of-plane anisotropy constants.

Further details of the Kittel fit parameters along with the values of anisotropic constants can be found in Section S3, Supporting Information. The effective damping (α_{eff}) constant is then extracted employing the following relation[48,50]

$$\alpha_{eff} = \frac{2}{\gamma \tau \left(2H\cos \left(\theta_H - \theta_M \right) + H_a + H_b \right)} \tag{5}$$

In Figure 3c we have shown the uniform precessional mode frequencies as obtained from sample 1 at different bias mag-

ADVANCED
SCIENCE NEWS
www.advancedsciencenews.com

ADVANCED
QUANTUM
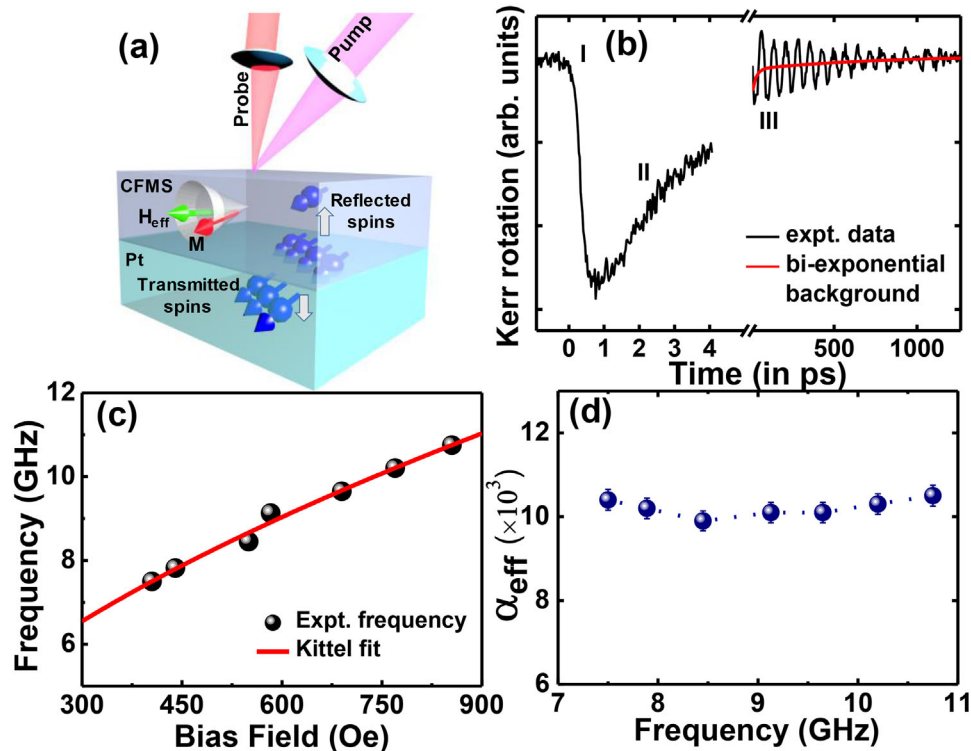TECHNOLOGIES
www.advquantumtech.com

Figure 3. Spin pumping phenomenon and estimation of Gilbert damping' a) Schematic representation of spin pumping mechanism in CFMS/Pt interface measured employing non-collinear pump-probe arrangement. b) Three different regimes present in a typical TRMOKE data from the MgO(sub)/Cr(20 nm)/CFMS(10 nm)/Pt(5 nm)/Al(2 nm) heterostructure at H = 1.0 kOe. The bi-exponential background fit is shown by solid red line. c) Bias field dependence of the precessional frequency measured for sample S1 fitted with Kittel formula. d) Effective damping constant extracted for sample S1 showing nearly frequency-independent values.

netic field strengths. The field dependent dynamics has been fitted with the Kittel formula given by Equation (2) to extract the K_2, K_4 and K_z. We have also extracted α_{eff} at different bias magnetic field strengths. A plot of α_{eff} versus precession frequency for S1 shown in Figure 3d revealed that α_{eff} is nearly invariant with the precession frequency. As magnetic damping is highly correlated to atomic site ordering in CFMS,[43] a nearly frequency-independent value of α_{eff} can be attributed to a stable B2 structure observed for the studied samples and indicates the absence of any significant amount of inhomogeneous anisotropy distribution and TMS[51] due to the presence of surface and volume impurities.[44] Nevertheless, we have extracted the precise contribution of TMS later in this article.

2.4. Modulation of Damping as a Route to Probe Spin Pumping

In an FM/NM heterostructure, apart from the intrinsic Gilbert damping, there can be various other physical mechanisms contributing to the magnetic damping such as spin pumping, two-magnon scattering, spin memory loss, etc. In a non-local contribution to damping like spin pumping, the FM layer acts as a source of spin current and the optically induced spin current in the FM layer flows through the FM/NM interface and finally dissipates in the adjacent NM layer acting as an absorption medium for spin current or a spin sink. This leads to an enhancement in the effective damping. This phenomenon is theoretically mod-

eled by Tserkovnyak et al., using a modified Landau–Lifshitz Gilbert equation given below[13]

$$\frac{d\vec{m}}{dt} = -\gamma \left(\vec{m} \times \vec{H}_{eff} \right) + \alpha_0 \left(\vec{m} \times \frac{d\vec{m}}{dt} \right) + \frac{\gamma}{VM_s} \vec{I}_s \quad (6)$$

Here, α_0 is the intrinsic Gilbert damping and V is the volume of the FM layer. The net spin current $\vec{I}_s$ consists of a DC contribution $\vec{I}_s^0$ which is null for the present case, pumped spin current $\vec{I}_s^{pump}$ from FM layer and a spin backflow current $\vec{I}_s^{back}$ from NM layer to FM layer since a practical NM material might not act as an ideal spin sink. Thus

$$\vec{I}_s = \vec{I}_s^0 + \vec{I}_s^{pump} + \vec{I}_s^{back} \quad (7)$$

The effect of a backflow of spin current from the NM to FM layer can be quantified by β as[52,53]

$$\beta = \left[2\pi G_{\uparrow\downarrow} \sqrt{\frac{\epsilon}{3}} \tanh\left(\frac{t}{\lambda} \right) \right]^{-1} \quad (8)$$

which depends on the spin-diffusion length (λ) of the NM medium.

Here, ϵ is the spin-flip probability given by[54,55]

$$\epsilon = \left(\frac{Z_{Pt}e^2}{\hbar c} \right)^4 \quad (9)$$

**ADVANCED
SCIENCE NEWS**

www.advancedsciencenews.com

**ADVANCED
QUANTUM
TECHNOLOGIES**

www.advquantumtech.com

whose value is obtained as 0.105 using $Z_{Pt} = 78$ for platinum and $\frac{e^2}{\hbar c}$ is the fine structure constant $= 1/137$

However, the transport of spin current through the interface is characterized by intrinsic and effective spin-mixing conductances. The effective spin-mixing conductance takes care of the spin backflow factor, and as the thickness of the NM layer enhances, it approaches the intrinsic spin-mixing conductance asymptotically in the regime of no or negligible backflow current. In the ballistic spin transport approach, the relation between spin-mixing conductance and enhancement of damping can be modeled as[37,38]

$$G_{eff} = G_{\uparrow\downarrow} \left(1 - e^{-\frac{2t}{\lambda}} \right) \tag{10}$$

$$G_{eff} = \frac{4\pi d M_s \Delta\alpha}{g\mu_B} = \frac{4\pi d M_s}{g\mu_B} \left(\alpha_{eff} - \alpha_0 \right) \tag{11}$$

Since the ballistic model does not take the resistivity of the NM layer into consideration, an alternative model based on drift-diffusion framework[39,40] provides another functional relation between spin-mixing conductance and modulation of damping

$$G_{eff} = \frac{G_{\uparrow\downarrow}}{1 + \frac{e^2 \lambda \rho G_{\uparrow\downarrow}}{h} \coth\left(\frac{t}{\lambda}\right)} \tag{12}$$

where ρ is the resistivity of the NM and the reverse flow of the spin current is represented by the hyperbolic cotangent term present in the denominator.

Now, according to the spin Hall magnetoresistance model, the detected spin current at the NM layer is smaller than the spin current pumped out of the FM layer. This reduction can indicate many possible physical factors like the presence of local disorder and intermix at the FM/NM interface accompanied by electronic band mismatch etc. In the spin Hall magnetoresistance (SHM) model,[41] interfacial spin transparency (T) parametrizes all these hindrances and is correlated with G_{eff} by the following relation

$$T = \frac{G_{eff} \tanh\left(\frac{t}{2\lambda}\right)}{G_{eff} \coth\left(\frac{t}{\lambda}\right) + \frac{h}{2e^2 \lambda \rho}} \tag{13}$$

However, in the spin-transfer torque (STT)-based model the spin backflow factors are neglected. In the higher thickness regime of both the FM and NM layers the interfacial spin transparency attains the following form[42]

$$T = \frac{\frac{2G_{\uparrow\downarrow}}{G_{NM}}}{1 + \frac{2G_{\uparrow\downarrow}}{G_{NM}}} \tag{14}$$

where $G_{NM} = \frac{h}{e^2 \lambda \rho}$ refers to as the spin conductance for the platinum layer here.

In a heterostructure like the one under investigation, there could be other physical effects playing a role in the observed modulation of damping. The spin angular momentum exerted by the precessing spins in the FM layer can suffer a loss at the interface due to SML,[56] TMS etc. Whereas the spin-orbit coupling at the interface or proximity induced interfacial depolarization leads to the SML and consequent enhancement of damping, the creation of degenerate magnon modes from an initially

uniform FMR mode caused by the surface inhomogeneity scattering centers, leads to TMS effect.[57] Inclusion of these two effects into the effective damping gives the following modified set of expressions[19,58]

$$\alpha_{eff} = \alpha_0 + \alpha_{SP} + \alpha_{SML} + \alpha_{TMS} \tag{15}$$

$$\alpha_{eff} = \alpha_0 + \frac{g\mu_B}{4\pi d M_{eff}} \left(G_{eff} + G_{SML} \right) + \frac{\beta_{TMS}}{d^2} \tag{16}$$

G_{SML} is the spin conductance due to SML and β_{TMS} is the TMS coefficient depending on the defect density and perpendicular magnetic anisotropy in the FM layer.

2.5. Investigation of Thickness-Dependent Enhancement of Damping

The bi-exponential background subtracted precessional Kerr oscillations recorded at $H = 1.0$ kOe are presented in **Figure 4**a where the NM layer thickness is varied as $1 \leq t \leq 12$ nm for the sample Sub/Cr(20 nm)/CFMS(16 nm)/Pt(t)/Al(2 nm) (shown schematically in Figure 4b). A non-monotonic variation of α_{eff} is observed with t as presented in Figure 4c. In the lower thickness regime, that is, $t < 4$ nm, α_{eff} increases rapidly but for $t \geq 4$ nm, it starts to saturate and asymptotically approaches a value of 8.5×10^{-3}. This result is fitted using the ballistic model of spin transport with Equations (10) and (11) to estimate the intrinsic spin-mixing conductance, $G_{\uparrow\downarrow} = (6.51 \pm 0.21) \times 10^{15}$ cm^{-2} and the characteristic spin-diffusion length for platinum layer, $\lambda = 3.06 \pm 0.29$ nm. Moreover, we have further fitted our results employing Equations (11) and (12) as suggested by the spin diffusive model resulting in $G_{\uparrow\downarrow} = (1.23 \pm 0.11) \times 10^{16}$ cm^{-2} and $\lambda = 3.23 \pm 0.11$ nm as a fitting parameter. Unlike the ballistic approach that assumes a fast spin current transfer in the regime of $t \ll \lambda$, the resistivity of Pt is taken into consideration in the calculation of $G_{\uparrow\downarrow}$ by the diffusion model giving a higher estimate of spin-mixing conductance. The differences in the way the spin backflow is incorporated in both frameworks can be attributed to the differences in the estimated value of $G_{\uparrow\downarrow}$. However, the values obtained for spin-diffusion length using both the models are close enough and also are in agreement with the existing literature.[56,59] From Equation (9), we have calculated the spin-flip probability for platinum as $\epsilon = 0.105$ as mentioned above and the corresponding β as $(1.40 \pm 0.11) \times 10^{-16}$ cm^2 from Equation (8) for the sample with $t = 12$ nm. Here, β exhibits a strong width dependent modulation (up to 74%) and attains its maximum value of $(2.44 \pm 0.22) \times 10^{-16}$ cm^2 for the sample with the lowest Pt layer thickness, $t = 1$ nm.

Investigation of precessional dynamics for the other set of samples Sub/Cr(20 nm)/CFMS(d)/Pt(5 nm)/Al(2 nm) where the FM layer thickness (d) was varied as $10 \leq d \leq 20$ nm provides an avenue for direct experimental determination of G_{eff}. The time-resolved Kerr rotation data for these samples measured at $H = 1.0$ kOe are presented in **Figure 5**a. A plot of α_{eff} versus $1/d$ (Figure 5b) shows an almost linear behavior. The experimental result is fitted with the theoretical expression given by Equation (11) to extract the values of α_0 and G_{eff} to be 0.0039 ± 0.0004 and $(6.08 \pm 0.12) \times 10^{15}$ cm^{-2}, respectively.

Subsequently, to disentangle any possible contributions of SML and TMS at the interface from that of spin pumping in the

ADVANCED
SCIENCE NEWS

www.advancedsciencenews.com

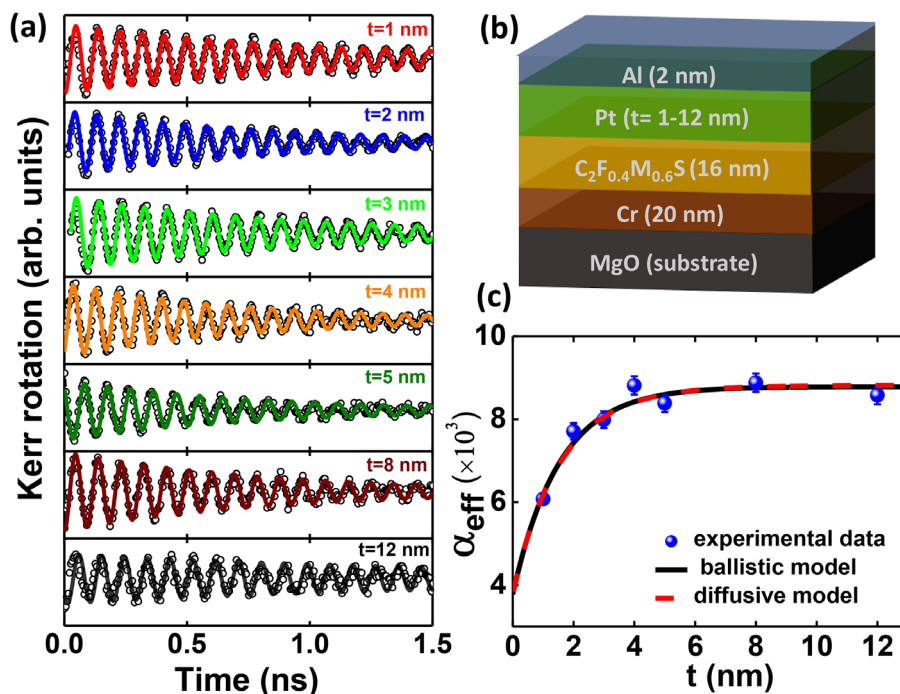**ADVANCED**
QUANTUM
TECHNOLOGIES

www.advquantumtech.com

Figure 4. Extraction of intrinsic spin-mixing conductance and spin-diffusion length. a) Background subtracted time-resolved Kerr rotation data for samples with Pt thickness $t = 1, 2, 3, 4, 5, 8,$ and 12 nm recorded at $H = 1.0$ kOe. b) Schematic representation of the corresponding sample with varying thickness of the Pt layer. c) Variation of α_{eff} as a function of t. The solid and dashed lines represent the theoretical fits employing the ballistic and drift-diffusive spin transport model, respectively, to extract the intrinsic spin-mixing conductance and the spin-diffusion length.
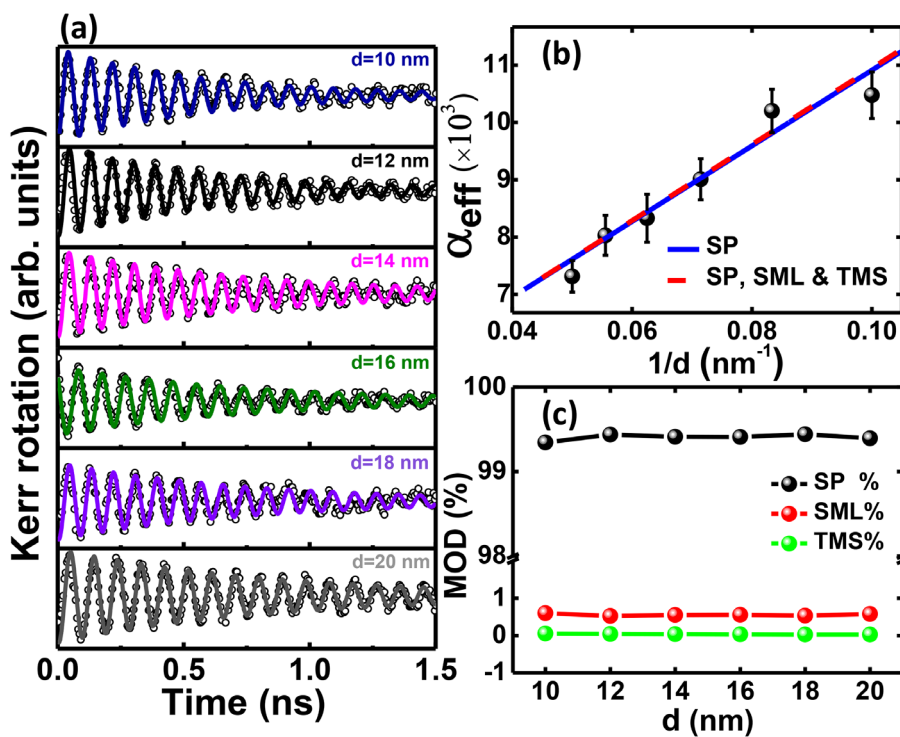

Figure 5. Estimation of effective spin-mixing conductance and intrinsic damping. a) Background subtracted time-resolved Kerr rotation data for samples with CFMS thickness of 10, 12, 14, 16, 18, and 20 nm obtained at $H = 1.0$ kOe. b) Enhancement of effective damping constant with inverse of CFMS layer thickness is shown. The blue solid line represents the theoretical fit considering spin pumping only, whereas red dashed line represents fitting with contributions from spin memory loss (SML) and two-magnon scattering (TMS) taken into consideration. c) Percentage contribution in modulation of damping (MOD) from spin pumping, SML and TMS across the thickness range of CFMS layer.

**ADVANCED
SCIENCE NEWS**

www.advancedsciencenews.com

**ADVANCED
QUANTUM
TECHNOLOGIES**

www.advquantumtech.com

Table 2. Comparison of effective spin-mixing conductance and interfacial spin transparency obtained from present work with the values reported in the literature.

NM/FM material systems	Spin-mixing conductance [$\times 10^{15}$ cm^{-2}]	Interfacial spin transparency
Material interfaces with Pt		
Pt/Py[18]	1.52	0.25
Pt/Co[18]	3.96	0.65
Pt/FM[42]	0.6–1.2	0.34–0.67
Pt/YIG[60]	0.3–1.2	NA
Pt/Fe[61,62]	2.0–4.4	NA
Pt/Co$_{50}$Fe$_{50}$[63]	2.5	NA
Material interfaces with Heuslers		
β-Ta/Co$_2$FeAl[64]	2.90	0.68
Co$_2$FeAl/Mo[65]	1.56	NA
MoS$_2$/Co$_2$FeAl[66]	1.49	0.46
Co$_2$FeAl/Cu/β-Ta[67]	3.40	NA
Material Interfaces with Heuslers and Pt		
Co$_2$MnSi/Pt[68]	6.5–9.0	NA
Co$_2$FeAl$_{0.5}$Si$_{0.5}$/Pt[69]	2.1–3.7	NA
Co$_2$Fe$_{0.4}$Mn$_{0.6}$Si/Pt [this work]	6.08	0.87

modulation of damping, we have further fitted the results using a modified expression for α_{eff} as given by Equation (16). From this fit, we have extracted the value of $G_{\text{SML}} = (3.21 \pm 0.15) \times 10^{13}$ cm^{-2} and the coefficient for TMS is found to be $\beta_{\text{TMS}} = (3.57 \pm 0.21) \times 10^{-18}$ cm^2 which shows that the contributions of SML and TMS in the modulation of damping are negligible in comparison to that of spin pumping. Their relative contributions are plotted in Figure 5c, which confirm that the effect of spin pumping is far more dominant for the systems under investigation. It is to be noted that the value of G_{eff} obtained for the CFMS/Pt interface is significantly higher than the value for other FM/NM heterostructures, as shown in **Table 2**, promoting this system as a strong candidate for spin-orbit torque (SOT)-based devices.

We have further measured the resistivity of the Pt layer and used G_{eff} as obtained above to extract the interfacial spin transparency, T. As T depends on the electronic band matching of the metals in an FM/NM junction, it is an electronic property of the interface and a higher value of T is always desirable for energy-efficient SOT applications. We have found $T = 0.84 \pm 0.03$ using the Equation (13) considering the SHM model, while Equation (14) from STT-based model yields $T = 0.87 \pm 0.02$ which is slightly higher than that obtained from SHM. From Table 2, it is evident that the interfacial spin transparency value that we obtained from the present study is highest among the available literature reports on various FM/NM systems involving heavy metals.

Interfacial spin transparency essentially expresses the probability of transfer of spins across the interface of ferromagnet and nonmagnet interface. As it is a function of effective spin-mixing conductance, it will highly depend on the spin-orbit coupling strength of the NM material involved. Apart from this, interface band structure matching, presence of lattice defects and dislocations, Fermi velocity are some of the crucial factors[66] governing

the efficiency of spin transport and thereby implicitly contribute to manipulation of spin transparency. The spin density of states (DOS) at the Fermi level directly correlates with the Gilbert relaxation parameter and the associated damping[70]

$$G \propto \xi^2 D\left(E_F\right) \tag{17}$$

Also, G has a linear relationship with damping

$$G = \gamma \alpha M_s \tag{18}$$

Therefore,

$$\alpha \propto \xi^2 D\left(E_F\right) \tag{19}$$

ξ, the SOC parameter is very small for CFMS and constant for Pt. Also, Pt being a metal will possess high DOS at the Fermi level. Thus, for Pt, both the high SOC strength and large occupancy at the Fermi level control the rapid dissipation of strong spin angular momentum inflow from the CFMS layer which strongly enhances the effective damping. Therefore, both the material's choice as well as careful engineering of the interface play crucial role in observed large T. The giant interfacial spin transparency value essentially suggests the ease of spin transfer through a favorable CFMS/Pt interface and ushers superior application potential of CFMS/Pt heterostructure in pure spin current-based devices.

3. Conclusion

We have extensively investigated spin pumping and related phenomena in the CFMS/Pt heterostructure employing a non-invasive and reliable all-optical time-resolved magneto-optical Kerr effect technique. A strong but linear enhancement of effective damping is observed with increasing CFMS layer thickness whereas an initial exponential rise followed by saturation in damping is found with a systematic variation of Pt layer thickness in the range of 1–12 nm. The relationship between the effective damping constant and the thickness of the CFMS layer has been modeled to extract the intrinsic Gilbert damping to be 0.0039 ± 0.0004 and effective spin-mixing conductance to be $(6.08 \pm 0.12) \times 10^{15}$ cm^{-2}. The results for variation of effective damping constant with the Pt thickness have been modeled employing ballistic spin transport as well as drift-diffusive based framework for spin transport to extract the intrinsic spin-mixing conductance values of $(6.51 \pm 0.21) \times 10^{15}$ cm^{-2} and $(1.23 \pm 0.11) \times 10^{16}$ cm^{-2}, respectively. Furthermore, we have isolated the contributions from spin memory loss and two magnon scattering to damping and found them to be negligible in comparison to spin pumping. The T value is also estimated to be 0.84 ± 0.03 and 0.87 ± 0.02 using the spin Hall magnetoresistance model and spin-transfer torque model, respectively. The value of T is one of the highest reported values in such FM/NM heterostructure so far. The large interfacial transparency in conjunction with the high value of effective spin-mixing conductance and small intrinsic Gilbert damping strongly place the CFMS/Pt heterostructure as a potential candidate for the SOT-based new generation storage and memory devices.

**ADVANCED
SCIENCE NEWS**

www.advancedsciencenews.com

**ADVANCED
QUANTUM
TECHNOLOGIES**

www.advquantumtech.com

4. Experimental Section

Sample Fabrication: Thin films of CFMS Heusler compound were deposited on a 20 nm thick buffer layer of Cr grown on the top of a single crystalline MgO (001) substrate at room temperature using ultra-high vacuum-compatible magnetron sputtering at a base pressure below 1×10^{-7} Torr. This was followed by an in situ annealing at 500 °C to promote the high-quality crystalline ordering of CFMS. After the in situ annealing for CFMS layer, a Pt layer was deposited on top at room temperature. The depositions were carried out typically at a rate of 0.01 Å s^{-1} with Ar pressure of 5 mTorr. Two series of films with stacks of MgO/Cr(20 nm)/CFMS(d)/Pt(t) were prepared for the present investigation. For series I (S1–S6), the nominal CFMS layer thickness was varied as $d = 10, 12, 14, 16, 18$, and 20 nm while maintaining a constant thickness of Pt layer at $t = 5$ nm. For series II (S7-S12), the Pt layer thickness was varied as $t = 1, 2, 3, 4, 5, 8$, and 12 nm, keeping a constant thickness of CFMS layer at $d = 16$ nm. A 2 nm thick capping layer made of Al was deposited on top of all the sample stacks to protect those from any external degradation including oxidation due to exposure in the atmosphere as well as to the femtosecond laser. For convenience, the sample names and nominal thickness values are listed in Table 1.

Measurements: In situ RHEED images of the samples were acquired to investigate the surface structural quality of the thin films. On the other hand, ex situ out-of-plane and tilted XRD patterns in θ–2θ geometry were measured to reveal the crystalline phase information and atomic site ordering in the thin films. AFM was used to probe the average surface roughness and the topography of the sample stacks and a standard four-probe technique was used to measure the resistivity. Static magnetic properties were measured using a VSM at room temperature. A custom-built all-optical TRMOKE magnetometer based on two-color optical pump-probe setup in a non-collinear geometry was employed to measure the ultrafast magnetization dynamics from the samples. Here the fundamental laser beam (wavelength, $\lambda = 800$ nm, full width at half maximum, FWHM ≈ 40 fs) from an amplified femtosecond laser source (Libra, Coherent Inc.) was split into two parts using a 30:70 beam splitter and the weaker part was used as probe and the second harmonic of the stronger part of this beam ($\lambda = 400$ nm, FWHM > 40 fs) was used as pump to excite the dynamics in the sample. The pump beam has a larger spot size (≈ 400 μm) on the sample surface as opposed to that of the probe beam (≈ 100 μm) ensuring the detection of local dynamics from a uniformly excited zone. The pump beam was obliquely incident on the sample, while the probe beam was incident normal to the sample plane so that the polar Kerr rotation is measured from the sample using a polarized beam splitter and two separate photodiodes. A variable magnetic field was applied to the sample at a small angle ($\approx 15°$) from the sample plane, the in-plane component of which (H) is referred to as the bias magnetic field. An optical chopper was used to modulate the pump beam at 373 Hz and Kerr rotation and reflectivity were recorded by two separate lock-in amplifiers in a phase-sensitive manner avoiding any possible breakthrough of one into another.

Supporting Information

Supporting Information is available from the Wiley Online Library or from the author.

Conflict of Interest

The authors declare no conflict of interest.

Author Contributions

A.B. conceptualized and supervised the project. T.S. and K.T. fabricated and characterized the thin film samples. K.D. and S.N.P. performed the measurements and analyzed the results in consultation with A.B. and S.P. K.D. prepared the manuscript in consultation with A.B. and T.S. All authors commented in the manuscript.

Data Availability Statement

The data that support the findings of this study are available from the corresponding author upon reasonable request.

[1] A. Hoffmann, *Phys. Status Solidi C.* **2007**, *4*, 4236.
[2] S. D. Bader, S. S. P. Parkin, *Annu. Rev. Condens. Matter Phys.* **2010**, *1*, 71.
[3] A. Hirohata, K. Yamada, Y. Nakatani, I. L. Prejbeanu, B. Dieny, P. Pirro, B. Hillebrands, *J. Magn. Magn. Mater.* **2020**, *509*, 166711.
[4] I. Žutić, J. Fabian, S. Das Sarma, *Rev. Mod. Phys.* **2004**, *76*, 323.
[5] C. Chappert, J.-V. Kim, *Nat. Phys.* **2008**, *4*, 837.
[6] F. Hellman, A. Hoffmann, Y. Tserkovnyak, G. S. D. Beach, E. E. Fullerton, C. Leighton, A. H. MacDonald, D. C. Ralph, D. A. Arena, H. A. Durr, P. Fischer, J. Grollier, J. P. Heremans, T. Jungwirth, A. V. Kimel, B. Koopmans, I. N. Krivorotov, S. J. May, A. K. Petford-Long, J. M. Rondinelli, N. Samarth, I. K. Schuller, A. N. Slavin, M. D. Stiles, O. Tchernyshyov, A. Thiaville, B. L. Zink, *Rev. Mod. Phys.* **2017**, *89*, 025006.
[7] J. E. Hirsch, *Phys. Rev. Lett.* **1999**, *83*, 1834.
[8] J. Sinova, S. O. Valenzuela, J. Wunderlich, C. H. Back, T. Jungwirth, *Rev. Mod. Phys.* **2015**, *87*, 1213.
[9] K. Uchida, S. Takahashi, K. Harii, J. Ieda, W. Koshibae, K. Ando, S. Maekawa, E. Saitoh, *Nature* **2008**, *455*, 778.
[10] W. Lin, M. Hehn, L. Chaput, B. Negulescu, S. Andrieu, F. Montaigne, S. Mangin, *Nat. Commun.* **2012**, *3*, 744.
[11] G. E. W. Bauer, E. Saitoh, B. J. van Wees, *Nat. Mater.* **2012**, *11*, 391.
[12] P. Sheng, Y. Sakuraba, Y. C. Lau, S. Takahashi, S. Mitani, M. Hayashi, *Sci. Adv.* **2017**, *3*, e1701503.
[13] Y. Tserkovnyak, A. Brataas, G. E. Bauer, *Phys. Rev. Lett.* **2002**, *88*, 117601.
[14] V. E. Demidov, S. Urazhdin, R. Liu, B. Divinskiy, A. Telegin, S. O. Demokritov, *Nat. Commun.* **2016**, *7*, 10446.
[15] Y. Fukuma, L. Wang, H. Idzuchi, S. Takahashi, S. Maekawa, Y. Otani, *Nat. Mater.* **2011**, *10*, 527.
[16] S. Maekawa, S. O. Valenzula, E. Saitoh, T. Kimura, *Spin Current*, Oxford University Press, Oxford **2017**.
[17] A. Brataas, Y. V. Nazarov, G. E. Bauer, *Phys. Rev. Lett.* **2000**, *84*, 2481.
[18] W. Zhang, W. Han, X. Jiang, S.-H. Yang, S. S. P. Parkin, *Nat. Phys.* **2015**, *11*, 496.

[19] S. N. Panda, S. Majumder, A. Bhattacharyya, S. Dutta, S. Choudhury, A. Barman, *ACS Appl. Mater. Interfaces* **2021**, *13*, 20875.

[20] H. Chudo, K. Ando, K. Saito, S. Okayasu, R. Haruki, Y. Sakuraba, H. Yasuoka, K. Takanashi, E. Saitoh, *J. Appl. Phys.* **2011**, *109*, 073915.

[21] B. B. Singh, K. Roy, P. Gupta, T. Seki, K. Takanashi, S. Bedanta, *NPG Asia Mater.* **2021**, *13*, 9.

[22] K. Elphick, W. Frost, M. Samiepour, T. Kubota, K. Takanashi, H. Sukegawa, S. Mitani, A. Hirohata, *Sci. Technol. Adv. Mater.* **2021**, *22*, 235.

[23] C. Guillemard, W. Zhang, G. Malinowski, C. de Melo, J. Gorchon, S. Petit-Watelot, J. Ghanbaja, S. Mangin, P. Le Fevre, F. Bertran, S. Andrieu, *Adv. Mater.* **2020**, *32*, e1908357.

[24] T. Kubota, S. Tsunegi, M. Oogane, S. Mizukami, T. Miyazaki, H. Naganuma, Y. Ando, *Appl. Phys. Lett.* **2009**, *94*, 122504.

[25] H.-x. Liu, Y. Honda, T. Taira, K.-i. Matsuda, M. Arita, T. Uemura, M. Yamamoto, *Appl. Phys. Lett.* **2012**, *101*, 132418.

[26] T. Seki, Y. Sakuraba, H. Arai, M. Ueda, R. Okura, H. Imamura, K. Takanashi, *Appl. Phys. Lett.* **2014**, *105*, 092406.

[27] T. Yamamoto, T. Seki, K. Takanashi, *Phys. Rev. B* **2016**, *94*, 094419.

[28] S. Picozzi, A. Continenza, A. J. Freeman, *Phys. Rev. B* **2002**, *66*, 094421.

[29] A. L. Kwilu, M. Oogane, H. Naganuma, M. Sahashi, Y. Ando, *J. Appl. Phys.* **2015**, *117*, 17D140.

[30] L. Bainsla, R. Yilgin, J. Okabayashi, A. Ono, K. Suzuki, S. Mizukami, *Phys. Rev. B* **2017**, *96*, 094404.

[31] C. Guillemard, S. Petit-Watelot, L. Pasquier, D. Pierre, J. Ghanbaja, J. C. Rojas-Sánchez, A. Bataille, J. Rault, P. Le Fèvre, F. Bertran, S. Andrieu, *Phys. Rev. Appl.* **2019**, *11*, 064009.

[32] B. Balke, G. H. Fecher, H. C. Kandpal, C. Felser, K. Kobayashi, E. Ikenaga, J.-J. Kim, S. Ueda, *Phys. Rev. B* **2006**, *74*, 104405.

[33] M. Oogane, T. Kubota, Y. Kota, S. Mizukami, H. Naganuma, A. Sakuma, Y. Ando, *Appl. Phys. Lett.* **2010**, *96*, 252501.

[34] A. Soumyanarayanan, N. Reyren, A. Fert, C. Panagopoulos, *Nature* **2016**, *539*, 509.

[35] S. Panda, S. Mondal, J. Sinha, S. Choudhury, A. Barman, *Sci. Adv.* **2019**, *5*, eaav7200.

[36] J. M. Shaw, H. T. Nembach, T. J. Silva, *Phys. Rev. B* **2012**, *85*, 054412.

[37] J. Foros, G. Woltersdorf, B. Heinrich, A. Brataas, *J. Appl. Phys.* **2005**, *97*, 10A714.

[38] J. Borge, I. V. Tokatly, *Phys. Rev. B* **2017**, *96*, 115445.

[39] C. T. Boone, H. T. Nembach, J. M. Shaw, T. J. Silva, *J. Appl. Phys.* **2013**, *113*, 153906.

[40] C. T. Boone, J. M. Shaw, H. T. Nembach, T. J. Silva, *J. Appl. Phys.* **2015**, *117*, 223910.

[41] Y. T. Chen, S. Takahashi, H. Nakayama, M. Althammer, S. T. B. Goennenwein, E. Saitoh, G. E. W. Bauer, *Phys. Rev. B* **2013**, *87*, 144411.

[42] C.-F. Pai, Y. Ou, L. H. Vilela-Leão, D. C. Ralph, R. A. Buhrman, *Phys. Rev. B* **2015**, *92*, 064426.

[43] S. Pan, S. Mondal, T. Seki, K. Takanashi, A. Barman, *Phys. Rev. B* **2016**, *94*, 184417.

[44] S. Pan, T. Seki, K. Takanashi, A. Barman, *Phys. Rev. Appl.* **2017**, *7*, 064012.

[45] T. Yamamoto, T. Seki, M. Kotsugi, K. Takanashi, *Appl. Phys. Lett.* **2016**, *108*, 152402.

[46] E. Beaurepaire, J. C. Merle, A. Daunois, J. Y. Bigot, *Phys. Rev. Lett.* **1996**, *76*, 4250.

[47] A. Barman, J. Sinha, *Spin Dynamics and Damping in Ferromagnetic Thin Films and Nanostructures*, Springer International Publishing, Cham, Switzerland **2018**.

[48] H. C. Yuan, S. H. Nie, T. P. Ma, Z. Zhang, Z. Zheng, Z. H. Chen, Y. Z. Wu, J. H. Zhao, H. B. Zhao, L. Y. Chen, *Appl. Phys. Lett.* **2014**, *105*, 072413.

[49] M. R. Karim, A. Adhikari, S. N. Panda, P. Sharangi, S. Kayal, G. Manna, P. S. A. Kumar, S. Bedanta, A. Barman, I. Sarkar, *J Phys. Chem. C* **2021**, *125*, 10483.

[50] S. Pan, S. Choudhury, J. Sinha, A. Barman, *J. Magn. Magn. Mater.* **2020**, *502*, 166545.

[51] Y. Fan, X. Ma, F. Fang, J. Zhu, Q. Li, T. P. Ma, Y. Z. Wu, Z. H. Chen, H. B. Zhao, G. Lüpke, *Phys. Rev. B* **2014**, *89*, 094428.

[52] Y. Tserkovnyak, A. Brataas, G. E. W. Bauer, *Phys. Rev. B* **2002**, *66*, 224403.

[53] M. D. Kaufmann, Ph.D., University of Göttingen, **2006**.

[54] H. Nakayama, K. Ando, K. Harii, T. Yoshino, R. Takahashi, Y. Kajiwara, K. Uchida, Y. Fujikawa, E. Saitoh, *Phys. Rev. B* **2012**, *85*, 144408.

[55] A. Azevedo, L. H. Vilela-Leão, R. L. Rodríguez-Suárez, A. F. Lacerda Santos, S. M. Rezende, *Phys. Rev. B* **2011**, *83*, 144402.

[56] J. C. Rojas-Sanchez, N. Reyren, P. Laczkowski, W. Savero, J. P. Attane, C. Deranlot, M. Jamet, J. M. George, L. Vila, H. Jaffres, *Phys. Rev. Lett.* **2014**, *112*, 106602.

[57] M. J. Hurben, C. E. Patton, *J. Appl. Phys.* **1998**, *83*, 4344.

[58] L. Zhu, D. C. Ralph, R. A. Buhrman, *Phys. Rev. Lett.* **2019**, *123*, 057203.

[59] L. Liu, T. Moriyama, D. C. Ralph, R. A. Buhrman, *Phys. Rev. Lett.* **2011**, *106*, 036601.

[60] M. Haertinger, C. H. Back, J. Lotze, M. Weiler, S. Geprägs, H. Huebl, S. T. B. Goennenwein, G. Woltersdorf, *Phys. Rev. B* **2015**, *92*, 054437.

[61] E. T. Papaioannou, P. Fuhrmann, M. B. Jungfleisch, T. Brächer, P. Pirro, V. Lauer, J. Lösch, B. Hillebrands, *Appl. Phys. Lett.* **2013**, *103*, 162401.

[62] S. Keller, L. Mihalceanu, M. R. Schweizer, P. Lang, B. Heinz, M. Geilen, T. Bracher, P. Pirro, T. Meyer, A. Conca, D. Karfaridis, G. Vourlias, T. Kehagias, B. Hillebrands, E. T. Papaioannou, *New J. Phys.* **2018**, *20*, 053002.

[63] Y. Li, F. Zeng, S. S.-L. Zhang, H. Shin, H. Saglam, V. Karakas, O. Ozatay, J. E. Pearson, O. G. Heinonen, Y. Wu, *Phys. Rev. Lett.* **2019**, *122*, 117203.

[64] S. Akansel, A. Kumar, N. Behera, S. Husain, R. Brucas, S. Chaudhary, P. Svedlindh, *Phys. Rev. B* **2018**, *97*, 134421.

[65] S. Husain, A. Kumar, V. Barwal, N. Behera, S. Akansel, P. Svedlindh, S. Chaudhary, *Phys. Rev. B* **2018**, *97*, 064420.

[66] S. Husain, A. Kumar, P. Kumar, A. Kumar, V. Barwal, N. Behera, S. Choudhary, P. Svedlindh, S. Chaudhary, *Phys. Rev. B* **2018**, *98*, 180404.

[67] A. Kumar, R. Gupta, S. Husain, N. Behera, S. Hait, S. Chaudhary, R. Brucas, P. Svedlindh, *Phys. Rev. B* **2019**, *100*, 214433.

[68] Y. Sasaki, S. Sugimoto, Y. K. Takahashi, S. Kasai, *AIP Adv.* **2020**, *10*, 085311.

[69] Y. Wu, Y.-L. Zhao, Q. Xiong, X.-G. Xu, Y. Sun, S.-Q. Zhang, Y. Jiang, *Chin. Phys. B* **2013**, *23*, 018503.

[70] V. Kamberský, *Can. J. Phys.* **1970**, *48*, 2906.